

Screening of Alzheimer's disease with multiwavelength Stokes polarimetry in a mouse model

Mariia Borovkova, Oleksii Sieryi, Ivan Lopushenko, Natalia Kartashkina, Jens Pahnke, Alexander Bykov, and Igor Meglinski, *Senior Member, IEEE*

Abstract—The minimum histological criterion for the diagnostics of Alzheimer's disease (AD) in tissue is the presence of senile plaques and neurofibrillary tangles in specific brain locations. The routine procedure of morphological analysis implies time-consuming and laborious steps including sectioning and staining of formalin-fixed paraffin-embedded (FFPE) tissue. We developed a multispectral Stokes polarimetric imaging approach that allows characterization of FFPE brain tissue samples to discern the stages of AD progression without sectioning and staining the tissue. The Stokes polarimetry approach is highly sensitive to structural alterations of brain tissue, particularly to the changes in light scattering and birefringence. We present the results of the label-free non-destructive screening of FFPE mouse brain tissue and show several polarization metrics that demonstrate statistically significant differences for tissues at different stages of AD.

Index Terms—Optical polarimetry, scattering, birefringence, A β plaques, Stokes vector.

I. INTRODUCTION

ALZHEIMER'S disease (AD) is a neurodegenerative disease and the most common cause of dementia [1]. Presently, the definite diagnosis of AD requires histological

analysis of brain tissue (postmortem) to detect the β -amyloid (A β) plaques and neurofibrillary tangles, the two major pathological hallmarks of AD. Senile plaques are composed of a dense crystalline nucleus and a corona/halo. The crystalline nucleus consists mainly of A β peptides, whereas the corona resembles degenerating neuronal axons and dendrites, inflammatory cells (microglia), astrocytes and more loosely packed A β [2], [3]. The A β in plaques consists mainly of 40 or 42 amino acids long peptides (A β 40, A β 42) [2], [3]. Neurofibrillary tangles are located intraneuronally and are composed of coiled hyperphosphorylated tau fibrils (PHF – paired helical filaments) which are currently detected by immunohistochemical staining (IHC) using tau-specific antibodies [4]–[6]. Neither plaques nor neurofibrillary tangles are adequately detected when only stained with hematoxylin and eosin (H&E) [4]–[6]. Silver stainings, e.g. Bielschowsky, which detect intracellular neurofibrillary tangles, axial cylinders of nerve fibers, and neuronal processes in senile plaques, are the most adequate techniques for the histologic diagnosis of AD [7]. The contours of neurons and their nuclei are impregnated against a light background, whereas in the soma of neurons, thin fibers of aggregated neurofibrils are revealed. A thin network of axons and their collaterals becomes

This work was supported by the Academy of Finland (grants 314369 and 325097), the ATTRACT project funded by the EC under Grant Agreement 777222, the INFOTECH strategic fund. The work of Mariia Borovkova was also supported by the European Union's Horizon 2020 research and innovation programme under the Marie Skłodowska-Curie grant agreement No.713606. The work of Jens Pahnke was supported by the following grants: Deutsche Forschungsgemeinschaft/ Germany (DFG 263024513); Latvian Council of Science/ Latvia (ShortAbeta Izp-2018/1-0275); HelseSØ/ Norway (2019054, 2019055); EEA grant/Norges grants (TAÇR TARIMAD TO100078); Norges forskningsrådet/ Norway (260786 PROP-AD, 295910 NAPI, PETABC); European Commission (643417). PROP-AD and PETABC are EU Joint Programme - Neurodegenerative Disease Research (JPND) projects. PROP-AD is supported through the following funding organizations under the aegis of JPND - www.jpnd.eu. The research was also partially supported by a grant under the Decree of the Government of the Russian Federation No. 220 of 09 April 2010 (Agreement No. 075-15-2021-615 of 04 June 2021) and the Ministry of Science and Higher Education of the Russian Federation within the framework of state support for the creation and development of World-Class Research Centers "Digital biodesign and personalized healthcare" № 075-15-2020-926 (*Corresponding authors: Mariia Borovkova; Igor Meglinski*).

Mariia Borovkova, Oleksii Sieryi, Ivan Lopushenko and Alexander Bykov are with the Optoelectronics and Measurement Techniques Unit, University of Oulu, 90570 Oulu, Finland (e-mails: mariia.borovkova@oulu.fi; olexii.sieryi@oulu.fi; ivan.lopushenko@oulu.fi; alexander.bykov@oulu.fi).

Natalia Kartashkina is with the Histology, Cytology and Embryology Department, I.M. Sechenov First Moscow State Medical University, 119991 Moscow, Russia (e-mail: kartashkina_n_i@staff.sechenov.ru).

Jens Pahnke is with the Department of Pathology, Section of Neuropathology, University of Oslo & Oslo University Hospital, Nydalen, N-0424 Oslo, Norway; the Department of Pharmacology, Faculty of Medicine, University of Latvia, Rīga, LV-1004 Latvia; the LIED, University of Lübeck, D-23538 Lübeck, Germany (e-mail: jens.pahnke@medisin.uio.no).

Igor Meglinski is with the College of Engineering and Physical Sciences, Aston University, Birmingham B4 7ET, U.K.; the Optoelectronics and Measurement Techniques Unit, University of Oulu, 90570 Oulu, Finland; Institute of Engineering Physics for Biomedicine (PhysBio), National Research Nuclear University MEPhI (Moscow Engineering Physics Institute), 115409 Moscow, Russia; Interdisciplinary Laboratory of Biophotonics, National Research Tomsk State University, 634050 Tomsk, Russia; V.A. Negovsky Scientific Research Institute of General Reanimatology, Federal Research and Clinical Center of Intensive Care Medicine and Rehabilitation, 141534 Moscow, Russia; Institute of Clinical Medicine N.V. Sklifosovsky, I.M. Sechenov First Moscow State Medical University, 129090 Moscow, Russia; Immanuel Kant Baltic Federal University, 236041 Kaliningrad, Russia (e-mail: i.meglinski@aston.ac.uk).

visible between the cells [8]. Alternatively, the fluorescent dye Thioflavin S, which is excited by the blue light and binds to β -sheets of amyloid fibrils, also detects senile plaques and can highlight neurofibrillary tangles [2], [4]. Various IHC methods are used in combination with routine techniques (H&E, Nissl stain, and silver impregnation methods) [7]. The A β in the nucleus of senile plaques shows apple-green birefringence when stained with the dye Congo red, indicating the presence of amyloid β -sheets in polarized light [2], [5].

In fact, currently used histological techniques are limited by a number of critical factors that may occur at any stage of the process, e.g. during removal, fixation or processing of tissue, as well as during embedding, sectioning, mounting and staining procedures [9], [10]. The examples of the factors that may lead to the deterioration of the histological images quality are: curls, tears, wrinkles, dents and/or stripes acquired during sectioning and/or mounting of fixed tissue; uneven dewaxing that may lead to uneven staining; cracks and/or distortion of the tissue pattern during microtome sectioning of frozen tissue samples; insufficient adherence of the tissue sections to the microscopic glass and/or deteriorated quality of dye solutions that may also lead to uneven staining and significant background staining. These artifacts may cause the multiple rounds of cutting and staining, incorrect interpretation of the images, or the destruction/uselessness of the tissue samples in the end. Thus, the current histological techniques are quite demanding, time-consuming, and laborious; as a result, the sampling is very limited. Moreover, the routine procedure provides only a 2D view of a tiny tissue fraction, additionally limiting the accuracy of the results interpretation and reproducibility. Thus, the result of histological analysis depends significantly on the quality of the samples preparation at each step and on the pathologist's skills, as only qualitative information is obtained. Currently, the studies on the application of machine-learning-based analysis methods to interpret histology images are striving to improve the accuracy and reliability of diagnostic pathology [11].

Recent studies have shown promising results in label-free imaging of A β plaques in thin slices of fixed or frozen brain tissue. The examples are stimulated Raman scattering (SRS) microscopy [12], Fourier-transform infrared spectroscopy (FTIR) [13], polarization-sensitive optical coherence microscopy (PS-OCM) [14], diffraction phase microscopy (DPM) [15], multiphoton microscopy [16], [17]. It has been demonstrated that brain tissue with AD exhibits higher inhomogeneity of refractive index, higher scattering coefficient, higher birefringence due to parallel alignment of fibrils in A β plaques and higher anisotropy of scattering [14], [15], [18]. In the previous studies, it has been demonstrated that polarimetry-based techniques have a high potential to implement the label-free, non-destructive express screening of brain tissues in order to facilitate the research on AD diagnostics and treatment [19]–[21].

In the current study, we used multiwavelength Stokes vector polarimetry to screen bulk formalin-fixed paraffin-embedded (FFPE) mouse brain tissue (brain hemispheres) without sectioning or staining to distinguish the severity of β -amyloidosis by analyzing the polarization properties of the light

backscattered from the tissue. The considered Stokes vector polarimetry approach based on circularly polarized illumination has been utilized in previous studies for screening of various biological tissues and tissue-like scattering media, e.g. detection of cancerous tissue, study of skin biomechanics, and optical clearing of biological tissues [22]–[28].

II. METHODS AND MATERIALS

The multiwavelength Stokes-vector imaging system developed in-house consists of illumination and detection arms and a XY translation stage that allows 2D spatial scanning of the sample. The experimental system is shown schematically in Fig. 1. In the illumination channel, the radiation produced by the supercontinuum fiber laser (Leukos Ltd., France) was filtered by the high-speed acousto-optic tunable filter (Leukos Ltd., France) in 450–650 nm range. The linearly polarized light beam emerging from the filter was transformed into right-circularly polarized (RHCP) light with the half-wave and quarter-wave plates (HWP, QWP) and was focused on the surface of a tissue block at 55° angle. The light backscattered from the sample was collected by a 20 \times objective lens at 30° angle with a variable distance away from the point of incidence (L_{SD}) [22]. A beam splitter (BS) placed in the light path split the beam with 10:90 ratio between the CMOS camera and the polarimeter respectively. The camera was used to control the focus position of the detection arm at the sample's surface. The rest of the beam was directed to the Stokes polarimeter (Thorlabs Ltd., USA). The diameter of the incident focused laser beam d_i was $\sim 15 \mu\text{m}$ (measured with a laser beam profiler (BeamMaster BM-7, Coherent)). The field of view of the objective lens in the detection arm d_d was $50 \mu\text{m}$. The angles of incidence and detection were optimized for elimination of specular reflection in the detected signal.

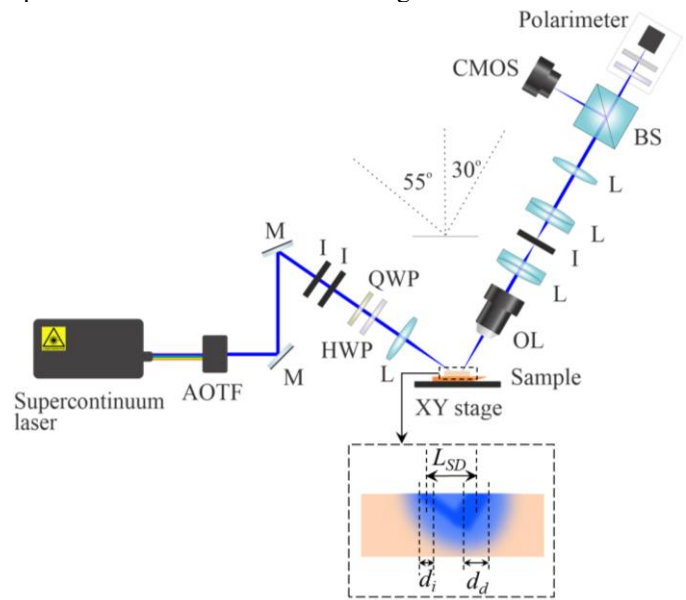


Fig. 1. Schematic layout of the Stokes vector polarimetry system (AOTF, acousto-optic tunable filter; M, mirror; I, iris; L, lens; OL, objective lens). Explanations are given in the text.

The scanning of the samples was performed over the $4.5 \text{ mm} \times 5.5 \text{ mm}$ area with a step $25 \mu\text{m}$ (in Y) and $5 \mu\text{m}$ (in X)

with the source-detector separation $L_{SD} = 0, 50, 100 \mu\text{m}$ and the wavelengths of the probing illumination $\lambda = 450, 550, 650 \text{ nm}$. At each scanning point, the full Stokes vector was measured ($S_0; S_1; S_2; S_3$), and the following parameters were calculated: the total degree of polarization ($\text{DoP} = \frac{\sqrt{S_1^2 + S_2^2 + S_3^2}}{S_0}$), the degree of polarization of linearly polarized light ($\text{DoLP} = \frac{\sqrt{S_1^2 + S_2^2}}{S_0}$), and the degree of polarization of circularly polarized light ($\text{DoCP} = \frac{\sqrt{S_3^2}}{S_0}$).

The paraffin blocks containing unstained fixed brain tissue from sacrificed APP-transgenic mice (APPPS-21, APPTg) [29] with different stages of β -amyloidosis were screened within the current study. The utilized APP-transgenic mouse models contain $A\beta$ (see Fig. 2(a,b)); the animals start with $A\beta$ deposition at an age of 40 days. In total, 24 brain hemispheres of mice of different age were investigated. All protocols of the breeding and the use of animals and all study procedures were performed in accordance with the 2010/63/EU Directive and the Norwegian Food Safety (Mattilsynet). The examined brain hemispheres were divided into two groups: less affected tissue (group I: 11 samples of animals 50-75 days of age), more affected tissue (group II: 13 samples of animals 175-200 days of age). Fig. 2(a,b) shows the histological images of brain tissue of animals of group I (a-1,a-2) and group II (b-1,b-2). $A\beta$ plaques are observed as dark brown spots throughout the brain tissue due to IHC staining [30]. The number, size, and density of $A\beta$ plaques is significantly higher in group II than in group I. Fig. 2(c) shows a photograph of a paraffin block, and Fig. 2(d) illustrates the number of samples per group.

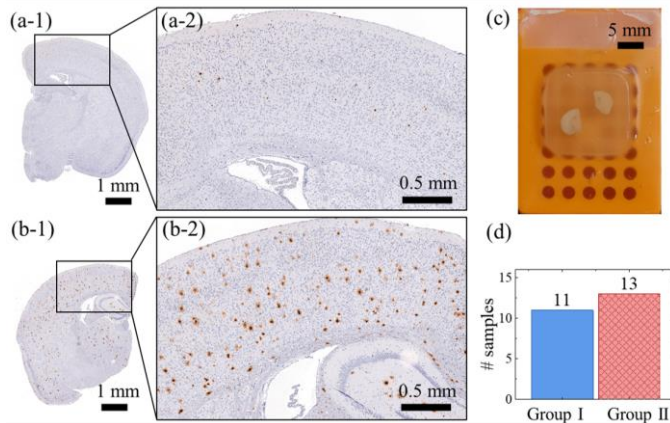


Fig. 2. Mouse brain samples. (a-1, a-2, b-1, b-2) Histological images of the brain hemispheres and magnified views of the marked areas of the samples from group I (a-1, a-2) and group II (b-1, b-2). (c) A photograph of a paraffin block. (d) The number of samples per group.

III. RESULTS AND DISCUSSION

The results of polarimetric imaging have shown that the polarization metrics of backscattered light are significantly different for the samples from the two groups. In particular, the DoP is found to be higher in most cases for the samples from group I than from group II at each incident wavelength and source-detector separation. Fig. 3 shows the DoP maps and

average DoP values of a sample from group I (a) and a sample from group II (b), measured at 450 nm incident wavelength with different values of source-detector separation: $L_{SD} = 0 \mu\text{m}$ (a-1, b-1, c-1), $L_{SD} = 50 \mu\text{m}$ (a-2, b-2, c-2), $L_{SD} = 100 \mu\text{m}$ (a-3, b-3, c-3). It was found that the increase of L_{SD} led to the decrease of the preserved DoP of light backscattered from the brain samples from both groups. This is a consequence of the enlargement of the sampling volume resulting from the increase of L_{SD} . Due to a larger sampling volume, light undergoes a higher number of scattering events which depolarize it. It should be pointed out that the DoP of light backscattered from the brain tissue decreased dramatically with the increase of L_{SD} , whereas this parameter remained the same for paraffin (see Fig. 3(a,b)). This is explained by the low light scattering by paraffin compared to scattering by the tissue. The increase of depolarization ($1 - \text{DoP}$) of light backscattered from paraffin was notable at $L_{SD} > 250 \mu\text{m}$.

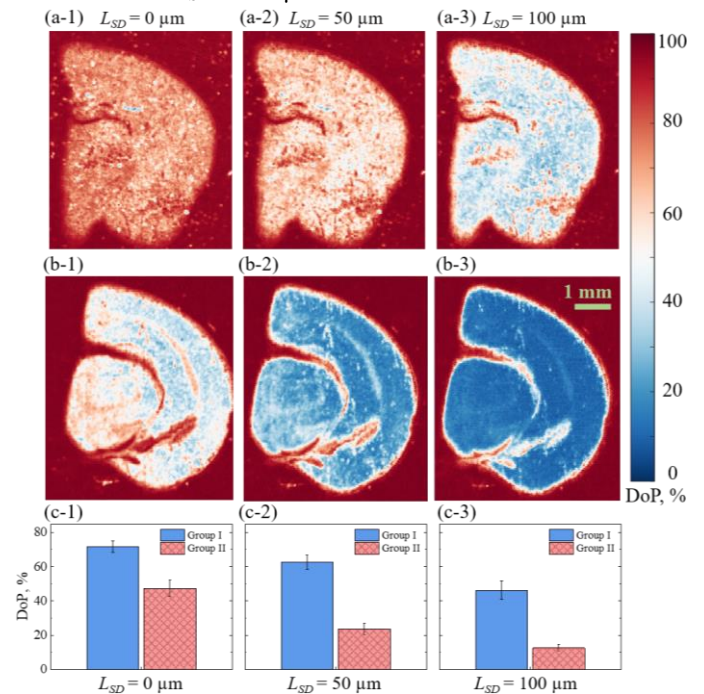


Fig. 3. DoP maps for samples from group I (a-1, a-2, a-3) and group II (b-1, b-2, b-3) and bar plots of DoP mean value (c-1, c-2, c-3), measured at 450 nm incident wavelength with different source-detector separations: $L_{SD} = 0 \mu\text{m}$ (a-1, b-1, c-1), $L_{SD} = 50 \mu\text{m}$ (a-2, b-2, c-2), $L_{SD} = 100 \mu\text{m}$ (a-3, b-3, c-3). P -value < 0.001 .

It is observed in Fig. 3(a,b) that the light depolarization by the tissue from group I was lower than that of group II. This is an indication of the higher light scattering by the tissue from group II, compared to group I. Notably, the level of light depolarization by the tissue from group II, measured at $L_{SD} = 0 \mu\text{m}$, was equivalent to the level of light depolarization by the tissue from group I, measured at $L_{SD} = 100 \mu\text{m}$. This indicates the enhancement of light scattering with the progression of the disease that has been also demonstrated in previous studies [15]. Thus, it is believed that the higher concentration of $A\beta$ protein and its aggregations is responsible for the increase of scattering within the brain tissue [18].

For the quantitative analysis of all acquired polarization

properties, the regions containing brain tissue were selected from the DoP image. The selection was performed individually for each measurement. The selection of spatial zones in DoP images was transferred to images of all other parameters obtained at the same measurement. The data inside the marked borders were processed and statistically analyzed.

Fig. 4 shows the comparison of each polarization metric (averaged within each sample) measured from the two groups of samples at 450 nm incident wavelength with $L_{SD} = 0, 50, 100 \mu\text{m}$. The compared polarization characteristics are DoP, DoLP, DoCP and three last components of the Stokes vector of a completely polarized part of the detected light (i.e., normalized by $S_0 \cdot \text{DoP}$) [31]. The Mann-Whitney test was used to assess the statistical significance of the differences in the considered parameters between the two groups of samples with the confidence interval of at least 95%. The limit of P -values is listed in the corresponding graphs. Refer to the Supplementary document¹ for the analogous graphs for the data measured at 550 and 650 nm incident wavelengths and for the calculated P -values of each comparison.

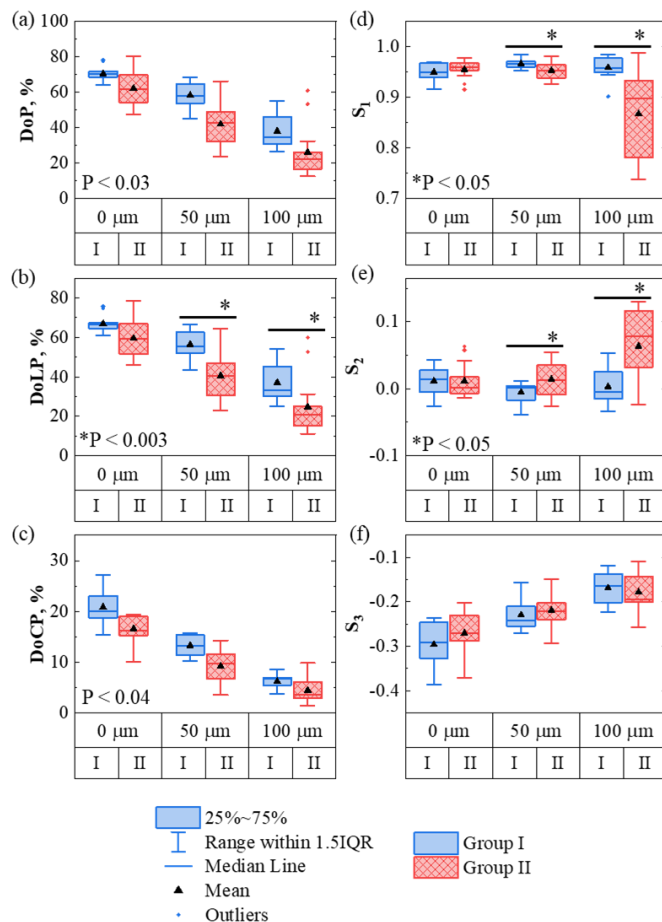


Fig. 4. Comparison of the mean values of (a) DoP (b) DoLP, (c) DoCP, (d) S_1 , (e) S_2 , (f) S_3 for the samples from the two groups, measured at 450 nm incident wavelength with $L_{SD} = 0, 50, 100 \mu\text{m}$. The analogous graphs for the data measured at 550, 650 nm incident wavelengths could be found in the Supplementary document.

¹ Supplementary materials are available in the supporting documents /multimedia tab.

The results presented in Fig. 4 show that the state of polarization (SoP) of light backscattered from all samples measured with all L_{SD} values was left-handed elliptical polarization. The increase of L_{SD} had a significant impact on all considered polarization metrics. As the Fig. 4(a) shows, the DoP of light backscattered from the tissue naturally decreased with the increase of L_{SD} . The same tendency was observed for DoLP and DoCP (Fig. 4(b,c)). The DoP, DoLP, DoCP of light scattered from the samples from group I were higher than the same parameters measured for the samples from group II at each measurement configuration (see Fig. 4(a,b,c)). Notably, the differences in DoP and DoCP between the two groups of samples were statistically significant with every value of L_{SD} ; the differences in DoLP were statistically significant at $L_{SD} \geq 50 \mu\text{m}$. The comparison of values of DoLP and DoCP demonstrates that the linear polarization was preserved by the tissues from both groups better than the circular polarization in the same measurement configuration. This phenomena has been observed in previous studies for biological tissues measured in backscattering configuration; it indicates that the tissue exhibits higher Rayleigh scattering than Mie scattering [32], [33].

The values of the Stokes vector components S_1 and S_2 were similar at $L_{SD} = 0, 50 \mu\text{m}$, but demonstrated high dispersion at $L_{SD} = 100 \mu\text{m}$ for both groups of samples (see Fig. 4(d,e)). At $L_{SD} = 0$, the values of S_1 and S_2 were similar for the samples from the two groups (see Fig. 4(d,e)). However, at $L_{SD} \geq 50 \mu\text{m}$, the values of S_1 became notably lower for the samples from group II than for the samples from group I, while the opposite relation was true for S_2 (see Fig. 4(d,e)). These differences were found statistically significant. The values of S_3 grew with the increase of L_{SD} ; the differences between them for the samples from different groups were moderate (see Fig. 4(f)).

The analysis of DoLP and DoCP decay is shown in Fig. 5. The data points were well approximated by a linear fit (adjusted $R^2 > 0.95$). It was found that the DoLP decays faster than the DoCP with the increase of L_{SD} for both groups of samples. The higher relative decay of linear polarization compared to circular polarization with the increase of scattering has been also demonstrated in previous studies [34].

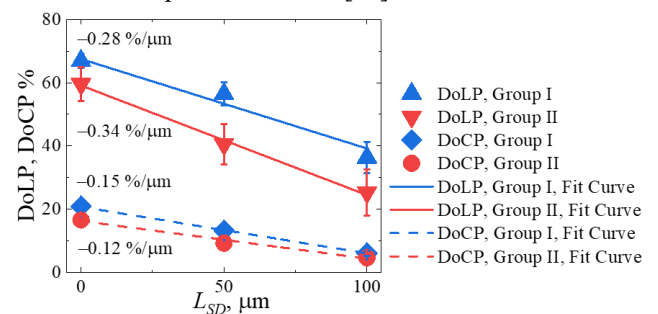


Fig. 5. Decline of DoLP and DoCP with the increase of L_{SD} for the two groups of samples and linear fit of the data points (450 nm incident wavelength). The numbers next to fit curves characterize the slopes.

Table 1 summarizes the results obtained at 450, 550, 650 nm incident wavelengths with $L_{SD} = 0, 50, 100 \mu\text{m}$. Table 1 shows

TABLE I
THE DIFFERENCES BETWEEN THE MEAN VALUES Z OF DISTRIBUTIONS OF POLARIMETRIC PROPERTIES (IN %).

Incident wavelength		$\lambda = 450 \text{ nm}$			$\lambda = 550 \text{ nm}$			$\lambda = 650 \text{ nm}$		
$L_{SD}, \mu\text{m}$		0	50	100	0	50	100	0	50	100
Difference between two groups as $\frac{Z(\text{GI})-Z(\text{GII})}{Z(\text{GI})} \cdot 100\%$	S_1	+0.6	-1	-8	+0.6	-2	-18	-0.3	-6	-23
	S_2	0	+1	+3	-1	+3	+4	-1	+1	+3
	S_3	+9	+5	-7	+4	+4	-8	+0.5	-10	-5
	DoP	-12	-28	-29	-10	-26	-26	-12	-24	-22
	DoLP	-11	-28	-30	-10	-26	-30	-12	-26	-28
	DoCP	-20	-31	-23	-15	-27	-20	-13	-18	-14

GI: group I, GII: group II. The statistically significant differences at $P < 0.05$ level are highlighted.

the differences in Z (the mean values of each measurement averaged within a group) of each considered polarimetric property between the two groups. The values that illustrated statistically significant differences at $P < 0.05$ level are highlighted in the table. It is observed that the differences in all parameters became larger with the growth of L_{SD} at all wavelengths, as the increase of the sampling volume led to the increase of the contribution of the polarimetric response of the tissue inner structure in the detected signal. The differences in the optical properties of the tissue from the two groups were therefore manifested more prominently at $L_{SD} \geq 50 \mu\text{m}$.

Fig. 6 demonstrates the Stokes vectors measured from the two groups of samples mapped on the Poincaré sphere. It is observed that the differences in SoP of light backscattered from the samples are attributed mostly to DoP, however, at $L_{SD} \geq 50 \mu\text{m}$, the distinction in S_{1-3} is evident (Fig. 6(a,c)).

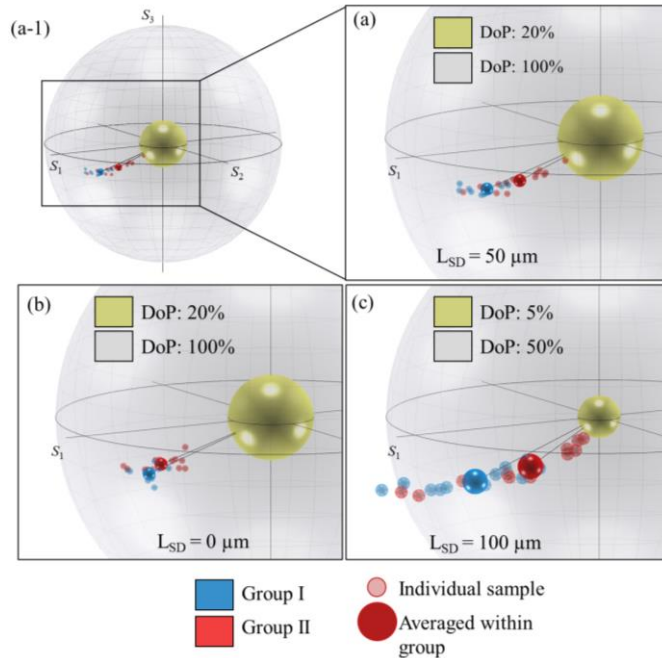


Fig. 6. Stokes vectors mapped on the Poincaré sphere with respect to DoP. (a-1) Full view of the Poincaré sphere with data points measured with $L_{SD} = 50 \mu\text{m}$, $\lambda = 650 \text{ nm}$. (a) Magnification of the sphere in (a-1). (b) Magnified part of the Poincaré sphere with data points measured with $L_{SD} = 0 \mu\text{m}$, $\lambda = 450 \text{ nm}$. (c) Magnified part of the Poincaré sphere with data points measured with $L_{SD} = 100 \mu\text{m}$, $\lambda = 650 \text{ nm}$.

Based on the results shown in Fig. 6(c), the value of birefringence was estimated using the relation $\Delta n = \delta\lambda / 2\pi l$, where l is the average photon pathlength within tissue. For the measurement configuration $L_{SD} = 100 \mu\text{m}$ and $\lambda = 650 \text{ nm}$, the average photon pathlength was calculated with the aid of Monte Carlo computational modeling [35], [36] as $\sim 200 \mu\text{m}$. Thus, the magnitude of birefringence in brain tissue was estimated as $(7.6 \pm 2.2) \cdot 10^{-5}$ for group I and $(1.4 \pm 0.4) \cdot 10^{-4}$ for group II. The higher magnitude of birefringence observed in the samples from group II is explained by the growing presence of A β plaques in brain tissue with the later stage of AD. The birefringence of A β plaques has been demonstrated in the literature [5], [14], [19]. The obtained values of birefringence are in good correlation with the findings presented in previous studies [14], [19].

To expand the results of our study on human brain tissue, additional research needs to be performed. Though there are many similarities between the corresponding regions of the human and mouse brain in terms of architecture and cell types, there are also substantial differences [37], [38]. As the birefringence, which causes the phase retardation between orthogonally polarized light components, is inherent to the fibrous structure of A β plaques, it is observed both in mouse and human brain tissue [14], [19]. However, for the future development of the technique, extensive studies of the polarimetric response of human brain tissue should be performed.

IV. SUMMARY AND CONCLUSIONS

We demonstrate that the use of multiwavelength Stokes vector polarimetry allows label-free, contactless, quantitative characterization of unstained bulk FFPE mouse brain tissue at different stages of AD. The increase of the source-detector separation allows achieving higher contrast in the polarization properties of light backscattered from the two groups of tissues differently affected by AD. It was demonstrated that the total DoP, DoLP and DoCP are sensitive to the structural alterations at all considered measurement configurations, whereas the components of the Stokes vector demonstrate moderate differences between the samples from different groups at the source-detector separation over $50 \mu\text{m}$. The value of birefringence for the brain tissue was estimated as $(7.6 \pm 2.2) \cdot 10^{-5}$ for group I and $(1.4 \pm 0.4) \cdot 10^{-4}$ for group II.

The higher magnitude of birefringence observed in the samples of group II is explained by the growing presence of A β plaques which exhibit birefringence due to their fibrous substructure. The implementation of the described approach into clinical use would improve the routine histological analysis procedure by allowing express pre-evaluation of the disease stage using non-stained and non-sectioned blocks of FFPE tissue. Such express digital characterization would make the standard histological analysis procedure less time-consuming and more cost-efficient, facilitating the research on AD.

REFERENCES

- [1] S. Mcgirr, C. Venegas, and A. Swaminathan, "Alzheimers Disease: A Brief Review," *J. Exp. Neurol.*, vol. 1, no. 3, pp. 89–98, 2020, doi: 10.33696/neurol.1.015.
- [2] L. C. Walker, *Amyloid beta plaques*, vol. 1, no. 31. 2020.
- [3] R. A. Armstrong, "The molecular biology of senile plaques and neurofibrillary tangles in Alzheimer's disease," *Folia Neuropathol.*, vol. 47, no. 4, pp. 289–299, 2009.
- [4] D. J. Dabbs, Ed., *Diagnostic Immunohistochemistry: Theranostic and Genomic Applications*, 5th Ed. Elsevier, 2019.
- [5] F. Gray, C. Duyckaerts, and U. de Girolami, Eds., *Escourolle and Poirier's Manual of Basic Neuropathology*. New York: Oxford University Press, 2019.
- [6] W. Gomez, R. Morales, V. Maracaja-Coutinho, V. Parra, and M. Nassif, "Down syndrome and Alzheimer's disease: common molecular traits beyond the amyloid precursor protein," *Aging*, vol. 12, no. 1, pp. 1011–1033, Jan. 2020, doi: 10.18632/aging.102677.
- [7] I. A. Mavroudis *et al.*, "Morphological Changes of the Human Purkinje Cells and Deposition of Neuritic Plaques and Neurofibrillary Tangles on the Cerebellar Cortex of Alzheimer's Disease," *American Journal of Alzheimer's Disease & Other Dementias*, vol. 25, no. 7, pp. 585–591, Nov. 2010, doi: 10.1177/1533317510382892.
- [8] X. Du, X. Wang, and M. Geng, "Alzheimer's disease hypothesis and related therapies," *Transl. Neurodegener.*, vol. 7, no. 1, p. 2, Dec. 2018, doi: 10.1186/s40035-018-0107-y.
- [9] S. Taqi, S. Sami, L. Sami, and S. Zaki, "A review of artifacts in histopathology," *J. Oral Maxillofac. Pathol.*, vol. 22, no. 2, p. 279, 2018, doi: 10.4103/jomfp.JOMFP_125_15.
- [10] A. M. Gown, "Diagnostic Immunohistochemistry: What Can Go Wrong and How to Prevent It," *Arch. Pathol. Lab. Med.*, vol. 140, no. 9, pp. 893–898, Sep. 2016, doi: 10.5858/arpa.2016-0119-RA.
- [11] K. Bera, K. A. Schalper, D. L. Rimm, V. Velcheti, and A. Madabhushi, "Artificial intelligence in digital pathology — new tools for diagnosis and precision oncology," *Nat. Rev. Clin. Oncol.*, vol. 16, no. 11, pp. 703–715, Nov. 2019, doi: 10.1038/s41571-019-0252-y.
- [12] M. Ji *et al.*, "Label-free imaging of amyloid plaques in Alzheimer's disease with stimulated Raman scattering microscopy," *Sci. Adv.*, vol. 4, no. 11, p. eaat7715, Nov. 2018, doi: 10.1126/sciadv.aat7715.
- [13] C. R. Liao *et al.*, "Synchrotron FTIR reveals lipid around and within amyloid plaques in transgenic mice and Alzheimer's disease brain," *Analyst*, vol. 138, no. 14, pp. 3991–3997, 2013, doi: 10.1039/c3an00295k.
- [14] B. Baumann *et al.*, "Visualization of neuritic plaques in Alzheimer's disease by polarization-sensitive optical coherence microscopy," *Sci. Rep.*, vol. 7, no. 1, p. 43477, Apr. 2017, doi: 10.1038/srep43477.
- [15] M. Lee *et al.*, "Label-free optical quantification of structural alterations in Alzheimer's disease," *Sci. Rep.*, vol. 6, no. 1, p. 31034, Aug. 2016, doi: 10.1038/srep31034.
- [16] W. R. Zipfel, R. M. Williams, R. Christie, A. Y. Nikitin, B. T. Hyman, and W. W. Webb, "Live tissue intrinsic emission microscopy using multiphoton-excited native fluorescence and second harmonic generation," *Proc. Natl. Acad. Sci.*, vol. 100, no. 12, pp. 7075–7080, Jun. 2003, doi: 10.1073/pnas.0832308100.
- [17] S. Chakraborty, S.-T. Chen, Y.-T. Hsiao, M.-J. Chiu, and C.-K. Sun, "Additive-color multi-harmonic generation microscopy for simultaneous label-free differentiation of plaques, tangles, and neuronal axons," *Biomed. Opt. Express*, vol. 11, no. 2, p. 571, Feb. 2020, doi: 10.1364/BOE.378447.
- [18] P. J. Marchand *et al.*, "Visible spectrum extended-focus optical coherence microscopy for label-free sub-cellular tomography," *Biomed. Opt. Express*, vol. 8, no. 7, p. 3343, Jul. 2017, doi: 10.1364/BOE.8.003343.
- [19] L.-W. Jin *et al.*, "Imaging linear birefringence and dichroism in cerebral amyloid pathologies," *Proc. Natl. Acad. Sci.*, vol. 100, no. 26, pp. 15294–15298, Dec. 2003, doi: 10.1073/pnas.2534647100.
- [20] M. Borovkova *et al.*, "Evaluating β -amyloidosis progression in Alzheimer's disease with Mueller polarimetry," *Biomed. Opt. Express*, vol. 11, no. 8, p. 4509, Aug. 2020, doi: 10.1364/BOE.396294.
- [21] P. Schucht *et al.*, "Visualization of White Matter Fiber Tracts of Brain Tissue Sections With Wide-Field Imaging Mueller Polarimetry," *IEEE Trans. Med. Imaging*, vol. 39, no. 12, pp. 4376–4382, Dec. 2020, doi: 10.1109/TMI.2020.3018439.
- [22] M. A. Borovkova, A. V. Bykov, A. Popov, and I. V. Meglinski, "Role of scattering and birefringence in phase retardation revealed by locus of Stokes vector on Poincaré sphere," *J. Biomed. Opt.*, vol. 25, no. 05, p. 057001, May 2020, doi: 10.1117/1.JBO.25.5.057001.
- [23] V. V. Dremine *et al.*, "Imaging of early stage breast cancer with circularly polarized light," in *Tissue Optics and Photonics*, Apr. 2020, no. 11363, p. 1136304, doi: 10.1117/12.2554166.
- [24] M. A. Borovkova *et al.*, "The use of Stokes-Mueller polarimetry for assessment of amyloid- β progression in a mouse model of Alzheimer's disease," in *Optical Biopsy XVIII: Toward Real-Time Spectroscopic Imaging and Diagnosis*, 2020, p. 19, doi: 10.1117/12.2550795.
- [25] D. Ivanov *et al.*, "Colon cancer detection by using Poincaré sphere and 2D polarimetric mapping of ex vivo colon samples," *J. Biophoton.*, vol. 13, no. 8, p. e202000082, May 2020, doi: 10.1002/jbio.202000082.
- [26] I. Meglinski, C. Macdonald, A. Doronin, and M. Eccles, "Screening Cancer Aggressiveness by Using Circularly Polarized Light," in *Optics in the Life Sciences*, 2013, p. BM2A.4, doi: 10.1364/BODA.2013.BM2A.4.
- [27] C. Macdonald and I. Meglinski, "Backscattering of circular polarized light from a disperse random medium influenced by optical clearing," *Laser Phys. Lett.*, vol. 8, no. 4, pp. 324–328, Apr. 2011, doi: 10.1002/lapl.201010133.
- [28] B. Kunnen, C. Macdonald, A. Doronin, S. Jacques, M. Eccles, and I. Meglinski, "Application of circularly polarized light for non-invasive diagnosis of cancerous tissues and turbid tissue-like scattering media," *J. Biophoton.*, vol. 8, no. 4, pp. 317–323, 2015, doi: 10.1002/jbio.201400104.
- [29] R. Radde *et al.*, "A β 42-driven cerebral amyloidosis in transgenic mice reveals early and robust pathology," *EMBO Rep.*, vol. 7, no. 9, pp. 940–946, Sep. 2006, doi: 10.1038/sj.embor.7400784.
- [30] J. Steffen *et al.*, "Expression of endogenous mouse APP modulates β -amyloid deposition in hAPP-transgenic mice," *Acta Neuropathol. Commun.*, vol. 5, no. 1, p. 49, Dec. 2017, doi: 10.1186/s40478-017-0448-2.
- [31] R. A. Chipman, "Polarimetry," in *Handbook of Optics Vol. 2*, M. Bass, Ed. McGraw-Hill, New York, 1994, pp. 22.1-22.37.
- [32] A. Pierangelo *et al.*, "Ex-vivo characterization of human colon cancer by Mueller polarimetric imaging," *Opt. Express*, vol. 19, no. 2, pp. 1582–1593, Jan. 2011, doi: 10.1364/OE.19.001582.
- [33] V. Sankaran, J. T. Walsh, and D. J. Maitland, "Comparative study of polarized light propagation in biologic tissues," *J. Biomed. Opt.*, vol. 7, no. 3, pp. 300–307, 2002, doi: 10.1117/1.1483318.
- [34] N. Ghosh and I. Alex Vitkin, "Tissue polarimetry: concepts, challenges, applications, and outlook," *J. Biomed. Opt.*, vol. 16, no. 11, p. 110801, Nov. 2011, doi: 10.1117/1.3652896.
- [35] I. V. Meglinski, V. L. Kuzmin, D. Y. Churmakov, and D. A. Greenhalgh, "Monte Carlo simulation of coherent effects in multiple scattering," *Proc. R. Soc. A Math. Phys. Eng. Sci.*, vol. 461, no. 2053, pp. 43–53, Jan. 2005, doi: 10.1098/rspa.2004.1369.
- [36] A. Doronin, C. Macdonald, and I. Meglinski, "Propagation of coherent polarized light in turbid highly scattering medium," *J. Biomed. Opt.*, vol. 19, no. 2, p. 025005, Feb. 2014, doi: 10.1117/1.JBO.19.2.025005.
- [37] J. Li *et al.*, "Conservation and divergence of vulnerability and responses to stressors between human and mouse astrocytes," *Nat. Commun.*, vol. 12, no. 1, p. 3958, Dec. 2021, doi: 10.1038/s41467-021-24232-3.

- [38] R. D. Hodge *et al.*, “Conserved cell types with divergent features in human versus mouse cortex,” *Nature*, vol. 573, no. 7772, pp. 61–68, Sep. 2019, doi: 10.1038/s41586-019-1506-7.